https://doi.org/10.5194/wes-2026-39
Preprint. Discussion started: 23 February 2026

eawe european academy of wind energy
Open Access WIND ENERGY SCIENCE DISCUSSIONS

An experimental campaign to measure turbulence in the marine boundary layer

Jakob Mann[1], Ansh Patel[1], Mikael Sjöholm[1], Gunhild Rolighed Thorsen[1], Elliot Irving Simon[1], Lin-Ya Hung[2], and Julia Gottschall[2,3]

[1]DTU Wind and Energy Systems, Technical University of Denmark Risø Campus, 4000 Roskilde, Denmark
[2]Fraunhofer Institute for Wind Energy Systems IWES, Am Seedeich 45, 27572 Bremerhaven, Germany
[3]Faculty of Geosciences, University of Bremen, 28359 Bremen, Germany

Correspondence: Jakob Mann (jmsq@dtu.dk) and Ansh Patel (patel@dtu.dk)

Abstract. There is a lack of measurement data on the spatial structure of turbulence at heights greater than 100 m in the marine atmospheric boundary layer (MBL). Consequently, turbulence models like the Mann and Kaimal models, which are referred to in industry standards, have not been validated at the operational heights of large offshore wind turbines. To address this gap, we carried out an experimental campaign using a total of five lidars placed at two locations on the west coast of Denmark. This setup allowed us to measure the horizontal wind components at the intersections of the lidar beams which were 150 m to 250 m above the sea surface. As a result, lateral coherence can be assessed up to separations of 240 m. Due to differences in data quality from each lidar, the data availability at each intersection point was different, being in the range between 17% and 50% over the entire 360° sector. The statistics of the wind speed and direction showed trends that match the expectations for the measurement site and the vertical profiles of the wind speed were found to agree with simulation data from the Weather Research and Forecasting model (WRF). Thus, this measurement dataset can be used to test and validate turbulence models in the MBL at heights relevant for offshore wind turbines.

1 Introduction

Wind turbines are expected to continually increase in size over the next few decades. But there are many open research questions that must be addressed in order to bring about the expected decrease in cost of wind energy. One of these concerns the modelling of turbulence at the heights of multi-megawatt wind turbines (Kuik et al., 2016; Veers et al., 2023). The Kaimal (Kaimal et al., 1972) turbulence model was designed for onshore turbulence within the atmospheric surface layer and the Mann (1994) model was validated both on- and offshore, but only to heights less than 100 meters. Consequently, the assumptions behind these models may be violated at higher heights in the marine atmospheric boundary layer (MBL). For instance, both models assume that a large spectral gap exists between meso-scale and micro-scale turbulence. There is also a lack of measurement data

https://doi.org/10.5194/wes-2026-39
Preprint. Discussion started: 23 February 2026

eawe european academy of wind energy
Open Access WIND ENERGY SCIENCE DISCUSSIONS

against which, newer turbulence models (e.g. Segalini and Arnqvist, 2015; Chougule et al., 2017; Syed and Mann, 2024) can be validated.

Measurements of turbulence in the MBL have an extensive history in the field of atmospheric research (Weiler and Burling, 1967; Lenschow and Agee, 1976; Lenschow and Stankov, 1986; Wyngaard, 1992), and more recently, in the context of wind energy (Cheynet et al., 2017; Lampert et al., 2020; Putri et al., 2022; Syed and Mann, 2024). One of the first campaigns to measure turbulence at heights of modern wind turbines was carried out by Mann et al. (1991). They measured two-point co-spectra in the marine boundary layer using two meteorological masts (met-masts) placed on the island of Sprogø in the Great Belt, Denmark. Vincent et al. (2013) and Larsén et al. (2013) analysed spectra, co-spectra and coherence at low frequencies and at separations of more than one kilometer from two wind farms in the North and Baltic Seas. More recently, Cheynet et al. (2018) computed the spectra and vertical coherence over different stability regimes at heights up to 81 m above the German North Sea. They found that the Kaimal model mostly matched the observed spectra, except under very stable conditions when low frequency mesoscale turbulence was present in the frequency range under investigation. The vertical coherence was also found to be adequately described by the Davenport model (Davenport, 1961).

Due to the high cost of tall offshore met-masts, remote sensing techniques such as Light Detection and Ranging (lidar, see Sathe and Mann, 2013) have been increasingly used to measure turbulence at higher altitudes in the MBL (Cheynet et al., 2016, 2021; Angelou et al., 2023; Syed and Mann, 2024). Short-range continuous-wave dual lidars were deployed by Cheynet et al. (2016) on a bridge in Norway at a height of 55 m to measure lateral coherence, demonstrating that spatial averaging effects of lidars were negligible for these coherence measurements. Later a triple lidar configuration was used on the same platform, with the third lidar placed on the ground, to study coherence for both lateral and vertical separations (Nafisifard et al., 2023). Building on the dual lidar layout, Cheynet et al. (2021) used long-range scanning pulsed lidars to record spectra and lateral coherence up to 130 m above the Norwegian Sea in what was called the COTUR (COherence of TURbulence with lidars) campaign. However, high uncertainty in beam pointing directions limited the accuracy of their results. Angelou et al. (2023) and Syed and Mann (2024) used forward-looking nacelle lidars to measure lateral coherence at separations of around 100 m above the sea. These studies also observed meso-scale turbulence with the characteristic $-5/3$ slope (Nastrom et al., 1984; Lindborg, 1999) but were limited to line-of-sight measurements.

Here, we describe an experimental campaign aimed at measuring turbulence 150 m and 250 m above the North Sea. Our setup consists of five lidars placed on the western coast of Denmark. Moreover, the lidar beam directions are calibrated via drones to achieve a high pointing accuracy. It allows the lateral coherence in the “true" wind components to be measured at such heights, which has not been achieved before. The paper is structured as follows. Section 2 provides details of the experimental campaign including the site, instrumentation and calibration procedures. Section 3 describes what is contained in the publicly available data repository and Sect. 4 presents some quality checks on the data.

https://doi.org/10.5194/wes-2026-39
Preprint. Discussion started: 23 February 2026

eawe european academy of wind energy
Open Access WIND ENERGY SCIENCE DISCUSSIONS

2 The field campaign

2.1 Measurement layout overview

Like the COTUR experiment (Cheynet et al., 2021), we chose a coast facing the prevailing wind with a long uninterrupted offshore upstream fetch and relatively low terrain behind the shore, in order to emulate offshore conditions undisturbed by topography since a real offshore site would have been too expensive to install and operate. Such a coastal site was already located in the RUNE experiment (Floors et al., 2016), which investigated near-shore flow with lidars, and we reuse that site here. From the RUNE experiment, we already knew that landowners, tourists, and neighbours were positively inclined and would do no harm to the instrumentation. An additional practical advantage was the proximity to DTU's wind turbine test station at Høvsøre (Peña et al., 2016) that could provide some background meteorological information and the presence of technicians who could check the experiment regularly. Finally, this region of the North Sea is very close to planned and operating wind farms making the measurements even more relevant.

The experimental setup is shown in Figure 1. A total of five lidars were used in the experiment wherein two lidars were placed at the northern site close to the lighthouse in Bovbjerg and three lidars were present next to the church in Trans. The beams were pointed in westerly directions and had relatively low elevation angles (maximum 6.6° in phase 1 and 11.8° in phase 2) which meant that the plane of intersection lay about 150 m above the sea surface during the first phase of the campaign. The beam elevations were increased midway through the campaign, moving the intersection points to approximately 250 m. The precise elevation angles are described in Table 3 while the height of the intersection points are shown in Table 6 and a closer view of the intersection points is shown in Figure 2.

The timeline of the experimental field campaign that consisted of two staring configurations is shown in Table 1. During the measurement campaign the alignment of the scanners was checked using various methods. In April a RHI scan of the sea surface showed significant deviation (see Table 9) in the elevation angle and it was therefore decided to correct the elevation angle for staring configuration 2, by the error found from the RHI scans.

2.2 Measurement instrumentation and configurations

The southern instrumentation site (Trans Church) has a Vaisala CL31 ceilometer and three scanning pulsed lidar systems: one Vaisala WindCube Scan 200S, one Lumibird AllSky Streamline XR+, and one DTU Long-Range WindScanner 200S. The northern instrumentation site (Bovbjerg lighthouse) has two scanning pulsed lidar systems (one Streamline XR+ and one Long-Range WindScanner 200S). The positions of the equipment are in global GPS WGS84 UTM zone 32V coordinates and are listed in Table 2.

https://doi.org/10.5194/wes-2026-39
Preprint. Discussion started: 23 February 2026

eawe european academy of wind energy
Open Access WIND ENERGY SCIENCE DISCUSSIONS

Table 1. Timeline of the measurement campaign

Time	Event
September – December, 2023	Pre-calibrations
January, 2024	Deployment of equipment + first hard target mapping
1st of February, 2024	Starting lidar measurements in starring configuration 1
8th of February, 2024	Drone alignment (scanner configuration 1)
17th Of April, 2024	Hard target mapping (Drone alignment failed due to hardware problems)
22nd of April, 2024	RHI scans
25th of April, 2024	Starting lidar measurements in staring configuration 2 - offsets added to elevation angle
8th of May, 2024	Hard target mappings and starting LOS calibrations
17th of May, 2024	Starting lidar measurements in staring configuration 2
22nd of May, 2024	Starting LOS calibrations
3rd of June, 2024	Starting lidar measurements in staring configuration 2
21st of June, 2024	Hard target mapping
24th of June, 2024	RHI scans
25th of June, 2024	Drone alignment (scanner configuration 2)
26th of June, 2024	Decommissioning

Table 2. Positions of the equipment acquired using a Leica GS16 GNSS antenna in global GPS coordinates within UTM zone 32V. Positions refer to the center of the beam exit window.

Name	Type	Site	Easting [m]	Northing [m]	Height a.s.l. [m]
Zonda	Vaisala WindCube 200s	Church	445913.90	6261837.73	26.50
Chinook	Lumibird StreamLine XR+	Church	445915.15	6261838.74	26.28
Sterenn	DTU Windscanner 200S	Church	445916.94	6261839.58	26.37
Ceilometer	Vaisala CL31	Church	445916.34	6261837.31	26.97
Brise	DTU Windscanner 200S	Lighthouse	445825.33	6263507.17	42.92
Storm	Lumibird StreamLine XR+	Lighthouse	445824.08	6263508.42	42.87

https://doi.org/10.5194/wes-2026-39
Preprint. Discussion started: 23 February 2026

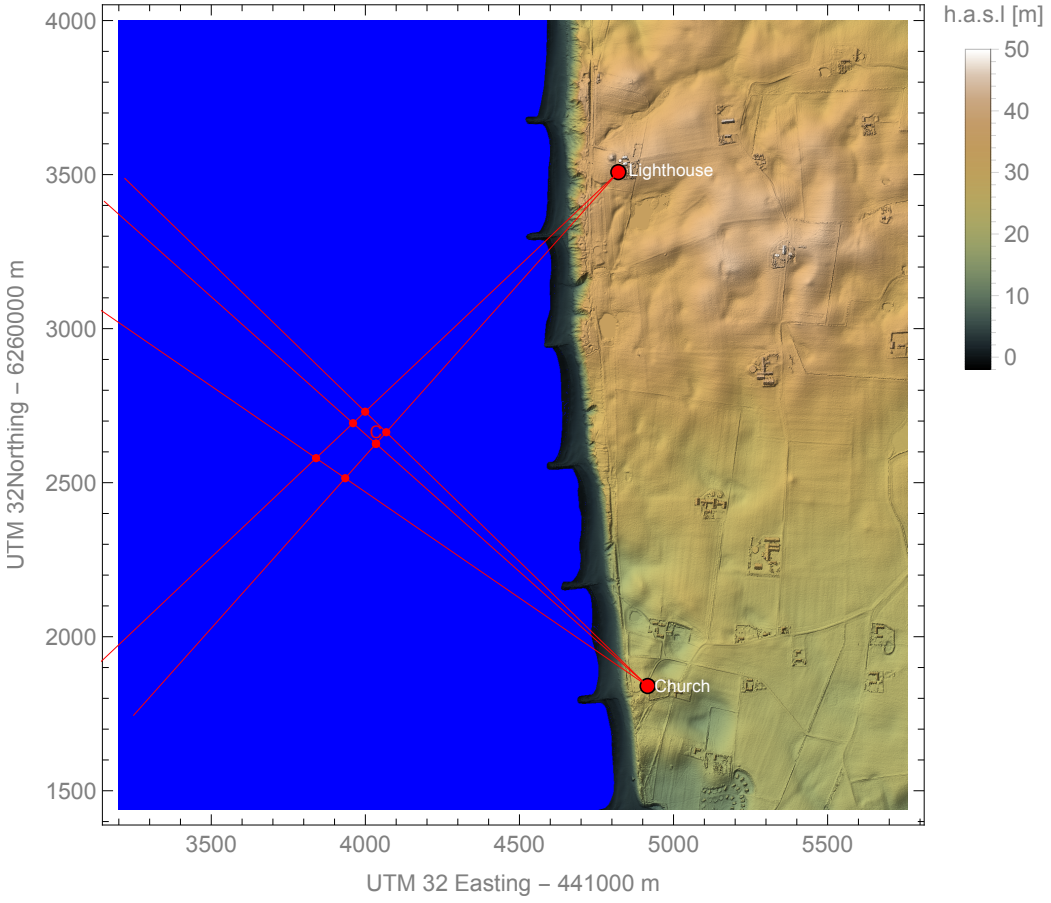

Figure 1. Top view of the experiment showing the two sites next to the church and the lighthouse. The lidar beams are shown in red while the dots indicate the intersection points. The center point where the beams meet at a 90° azimuth angle is indicated by a "C". The height above sea level is abbreviated by h.a.s.l.

The scanning lidar systems are configured to operate in staring (line-of-sight, LOS) mode, with fixed azimuth and elevation angle. During the campaign two different staring configurations were used. Table 3 shows the configurations of the different scanners.

2.3 Pre-campaign calibrations and testing

The pre-campaign calibration activities were carried out at DTU's Risø campus in Denmark, where five scanning lidars were deployed, four of which were used in the campaign (see Figure 4). The purpose of the pre-campaign testing was to ensure the correct functioning of the lidars and to determine if any offsets were present in the measurement data. As demonstrated in Simon et al. (2023), it is critical to perform these tests to ensure consistent and traceable performance of the lidar instruments.

https://doi.org/10.5194/wes-2026-39
Preprint. Discussion started: 23 February 2026

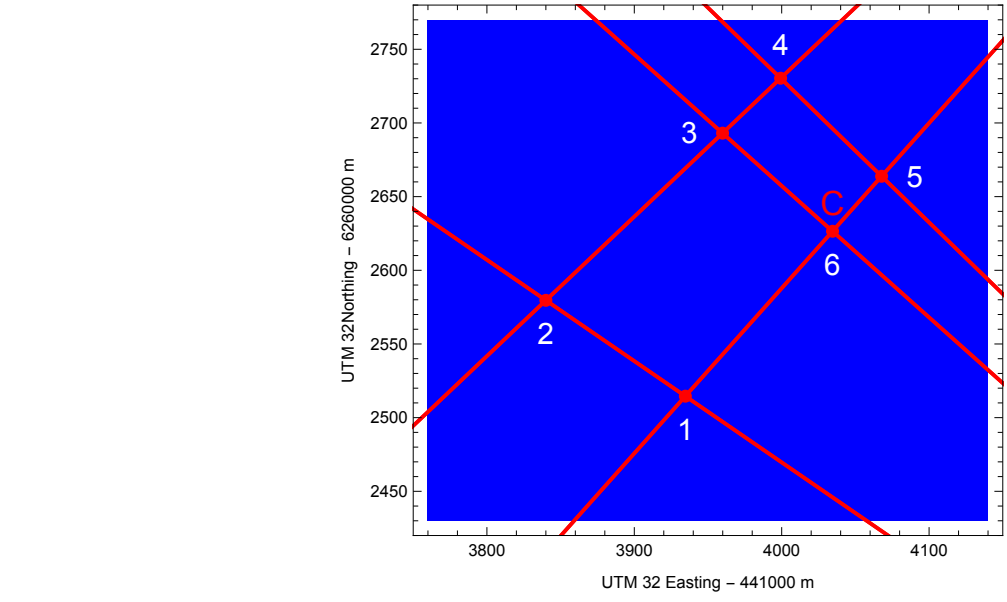

Figure 2. The intersection points of the lidar beams. The coordinates are given in Table 6.

Figure 3. Photos of the two sites where equipment was deployed in the field campaign (left: lighthouse, right: church).

Table 3. Summary of scanner setup. Beam directions are in the global coordinate system. The sampling rate for Zonda was 1 Hz and 2 Hz for the rest of the scanners.

		Range gate [m]			Beam direction 1 [°]		Beam direction 2 [°]	
Name	Type	Min	Max	Steps	Azimuth	Elevation	Azimuth	Elevation
Zonda (WLS200S-217)	WindCube 200S	50	1490	Varying	304.79	6.57	304.86	11.83
Chinook (S/N 242)	Streamline XR+	6 (useful from 50 m)	1504.5	1.5	311.92	5.98	311.92	10.72
Sterenn (WLS200S-06)	WindScanner	400	1500	5	314.24	5.75	314.22	10.30
Brise (WLS200S-10)	WindScanner	400	1500	5	221.92	5.18	221.92	9.94
Storm (S/N 212)	Streamline XR+	6 (useful from 50 m)	1504.5	1.5	226.65	5.66	226.59	10.78

https://doi.org/10.5194/wes-2026-39
Preprint. Discussion started: 23 February 2026

eawe european academy of wind energy
Open Access WIND ENERGY SCIENCE DISCUSSIONS

One of the scanners that were tested in the pre-campaign suffered a fatal laser error, and was therefore not used in the rest of the campaign. A replacement lidar (Zonda) was deployed in the measurement campaign in Jutland, but was not part of the pre-campaign testing. The five scanning lidars were deployed side-by-side at the turbine test station. The work began with calibrating the lidars' internal inclinometers to determine the value corresponding to the level position. This was accomplished by placing survey sticks with known positions across a range of azimuth positions and using each lidar's hard target mapping function to locate each stick in the lidar coordinate system. The levelling error was then determined, and the lidar was adjusted accordingly. This process was repeated until the stick positions were correct at all positions for all lidars.

Next, the lidars were set to measure in fixed LOS staring mode, with their beams placed in parallel, aimed and centred 1 m above the 118 m cup anemometer sensor on the 125 m tall Risø met-mast (Sogachev and Dellwik, 2017). The beam alignment was confirmed using hard-target mapping. However, the wind measurements taken during this period were of limited use due to hardware issues which were present on the Streamline XR+ systems. The issues included water ingress into one lidar due to improper weatherproofing of the lidar casing and a misadjusted focus position on both systems, which led to poor range and data availability during the tests. The Streamline systems were sent back to the manufacturer and repaired under warranty. Time synchronization was also an issue at the start of the tests for the WindScanner systems due to a software incompatibility with the Meinberg GPS module and Windows 10. The time-synchronization issue was resolved with a software update on October 18, 2023 at 09:09:20 UTC and the timestamps from this point forward are aligned and synchronized between all equipment.

Although the pre-campaign calibration was intended to be achieved through the line-of-sight inter-comparison of all (four) available scanning lidars, including a plausibility check against the met-mast, the results had to be collected during separate test periods. Due to the internal humidity and focus issues mentioned previously, the measurement range of the two Streamline systems did not consistently reach the required distance of the met-mast (1 km). The resulting offsets from the line-of-sight speed calibration are given in Table 4 and are further down compared to the post-calibration results. The left panel of Fig. 5 shows the regression between the two WindScanner systems (Brise and Sterenn), and the right panel shows the two Lumibird scanning lidars (Chinook and Storm). Both analyses indicate no significant offsets. For each lidar pair, a one-parameter linear fit yields $R^2 > 0.99$ and errors under 2%.

Fig. 6 compares the cup-anemometer wind speed projected onto the scanning lidar's line-of-sight (LOS). To minimize potential cross-wind component contamination, we retain data only when the wind direction is within $\pm 40^\circ$ of the LOS or within $\pm 40^\circ$ of the opposite direction (180° offset) according to International Electrotechnical Commission (2022). The wind direction selection also excludes the sector influenced by met-mast wake effects. Under these conditions, projection errors from the mast wind vane can be better distinguished and further compensated. To mitigate the impact of a wind direction offset on the projection, a sinusoidal function was fit to the wind speed ratio ($\mathrm{V_{LoS}}/\mathrm{V_{cup}}$) as a function of the azimuth angle in order to determine the lidar LOS angle in the wind vane coordinate system. This analysis uncovered a potential wind vane directional offset relative to the scanning lidar. The fitting process was applied on each system, and the outcomes from the system "Sterenn" were selected for consistency across systems. An angular offset of 5.8° was applied uniformly to all systems when using the met-mast cup anemometer as a reference. Sterenn was installed centrally among all scanning lidars, which justified the findings and choice of this angular offset to ensure consistency. The results shown in Fig. 6 reflect this filtering.

https://doi.org/10.5194/wes-2026-39
Preprint. Discussion started: 23 February 2026

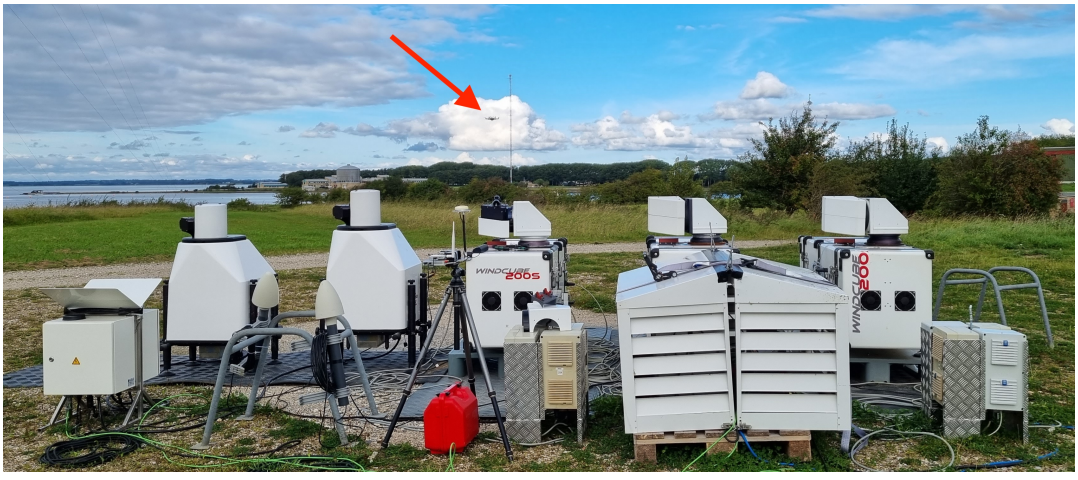

Figure 4. Photo of the pre-campaign lidar tests at Risø test station. A telescopic sight is fitted to the system in the center to help align the scan head with the met-mast and drone. The drone is flying and is visible in the center of the image at the red arrow.

Table 4. Results from the onshore pre-campaign line-of-sight speed calibration.

Scanner	LOS speed offset [m/s]
Brise-Sterenn	−0.30
Chinook-Storm	−0.17
Sterenn-Cup	0.30
Brise-Cup	0.19

The observation period for both Streamline/Lumibird systems have been shorter than those of WindScanners due to the failure mentioned.

2.3.1 Initial hard target mapping

The church and the lighthouse buildings were used as hard targets for aligning the azimuth direction of the scanners at the beginning of the campaign following the procedures of Vasiljević et al. (2016). Each of the hard targets were scanned using stacked sector plan position indicator (PPI) scans with sequential elevation angles, forming a "CNR mapper" as shown in Fig. 7. The elevation and azimuth angle for where the beam is pointing toward the tip of the lighthouse or church roof is determined. The positions of the church and the lighthouse in the global GPS coordinate system were obtained using the DHM (Danish Elevation Model) point cloud, which contains position data collected by laser scanning from an aircraft (see DHM).

The azimuth offset (ϕ_{offset}) is calculated as

$$\phi_{\text{offset}} = \phi_{\text{HT}} - \phi_{\text{scanner}} \tag{1}$$

https://doi.org/10.5194/wes-2026-39
Preprint. Discussion started: 23 February 2026

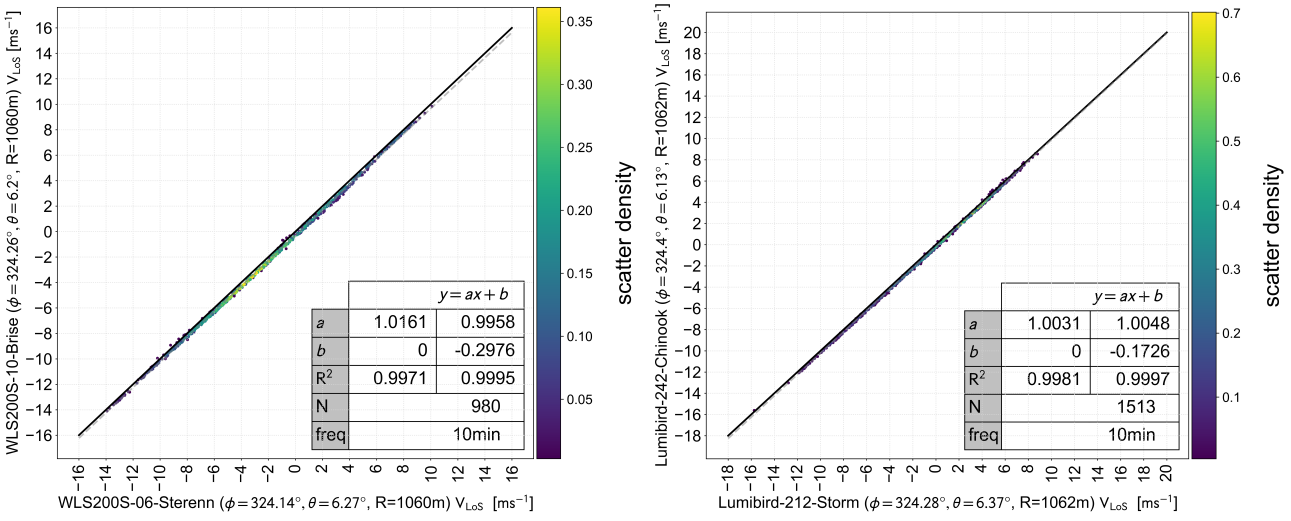

Figure 5. Regression analysis of the two pairs of scanning lidar systems during the pre-calibration test – left: WindScanner system; right: Streamline/Lumibird system. The range of comparison is roughly at the met-mast. Results of one and two-parameter fit are given in the table.

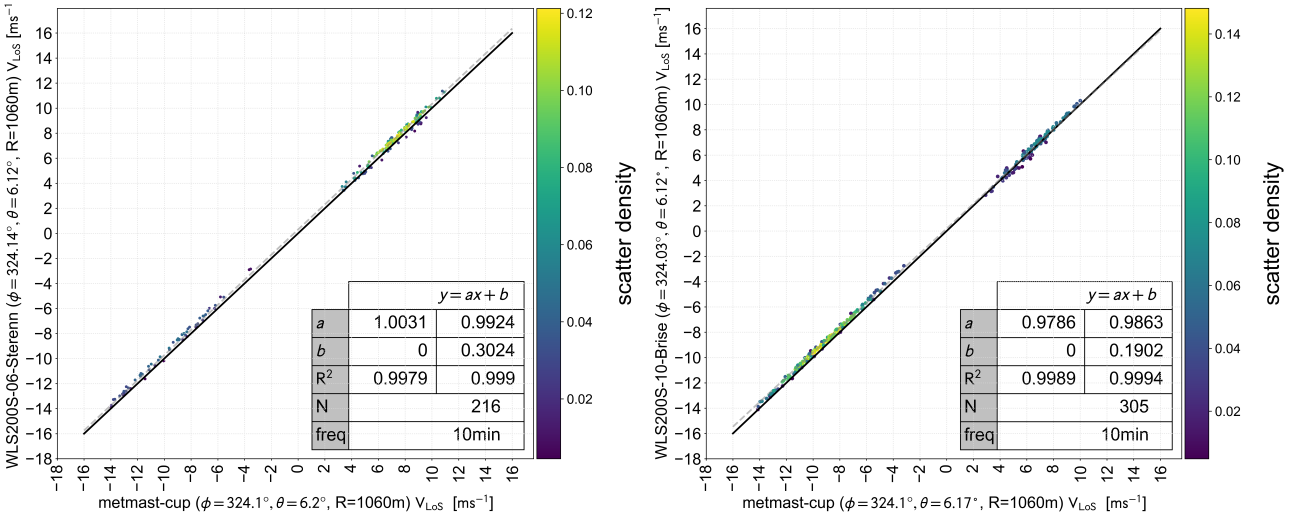

Figure 6. Regression analysis of the scanning lidar systems during the pre-calibration test against the metmast cup anemometer for the different models – left: Sterenn; right: Brise. Only wind direction from $\pm 40^\circ$ of the line-of-sight direction and corresponding angles of 180° apart have been kept for the analysis. Results of one and two-parameter fit are given in the table.

https://doi.org/10.5194/wes-2026-39
Preprint. Discussion started: 23 February 2026

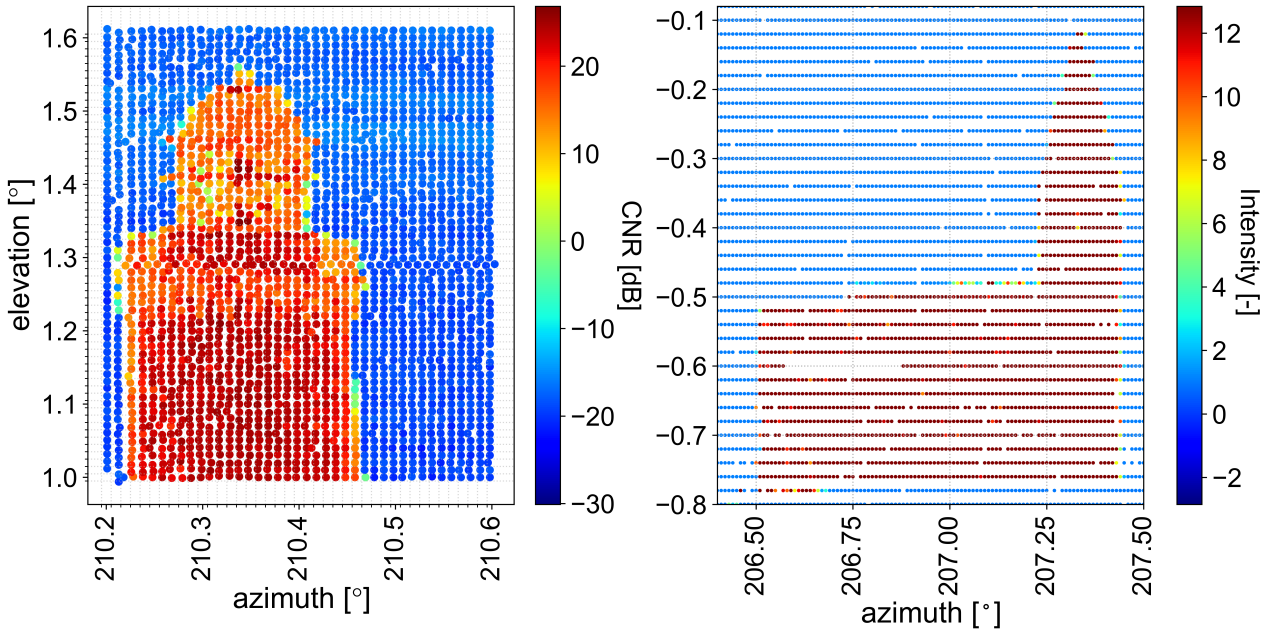

Figure 7. CNR mapper images of the lighthouse (left, Zonda) and church (right, Storm) used to align the beam positions. Stronger return signals appear in red, indicating that the lidar beams intersected a hard target.

Table 5. Results from the hard target mapping performed at the beginning of the campaign.

Name	Hard target	ϕ_{scanner} [°]	ϕ_{HT} [°]	ϕ_{offset} [°]
Zonda	Lighthouse	210.41	357.02	146.61
Chinook	Lighthouse	308.14	356.98	48.84
Sterenn	Lighthouse	219.60	356.92	137.32
Brise	Church	115.80	176.40	61.22
Storm	Church	207.35	176.36	-30.99

where ϕ_{HT} is the azimuth angle of the pointing direction from the scanner to the hard target in the global coordinate system and ϕ_{scanner} is the azimuth angle of the pointing direction from the scanner to the hard target in the scanner coordinate system. Note that the azimuth offsets determined via hard-target mapping were not directly implemented as a correction in the lidar software, due to the Lumibird systems not supporting this functionality. The azimuth offsets were applied in post-processing, which provided the correct alignment between global and lidar coordinate systems. Table 5 summarizes the results obtained from the hard target mapping. The initial results from hard-target scanning and wind measurements following deployment of the instruments indicate that the lidar systems were operating normally and were fit for use in the campaign.

https://doi.org/10.5194/wes-2026-39
Preprint. Discussion started: 23 February 2026

eawe european academy of wind energy
Open Access WIND ENERGY SCIENCE DISCUSSIONS

Table 6. Coordinates and height above sea level of the intersection points in experiment phase 1 and 2. The numbers in the first column refer to Figure 2.

Point	Lidars	z_m^1 [m]	z_m^2 [m]	UTM 32 Easting − 441000 [m]	UTM 32 Northing − 6260000 [m]
1	Zonda - Brise	163	275	3935	2515
2	Zonda - Storm	177	299	3840	2580
3	Chinook - Storm	161	268	3960	2693
4	Sterenn - Storm	155	258	3999	2730
5	Sterenn - Brise	145	241	4068	2664
6	Chinook - Brise	150	250	4034	2626

2.3.2 Drone-based pointing verifications

A method for verifying the correct pointing of the lidar beams using an aerial drone has been developed by DTU, and is described in Thorsen et al. (2023). The concept involves setting each lidar to stare at its intended measuring position, and flying a drone with a highly-accurate RTK (Real-Time Kinematic) positioning system into the beam path. The lidar is able to detect the presence of the drone along its beam path due to the high signal reflectivity indicated by the CNR value, similarly to traditional hard target mapping. By combining the lidar and drone data, it is possible to determine the actual beam position in global coordinates and either confirm the correct pointing, or quantify the offsets needed to correctly align the beams.

This exercise was performed twice during the FLOW campaign on all scanning lidars, both at the start and end of the measurements. Beyond obtaining two independent results of the pointing accuracy, repeating the exercise also provides an indication of the consistency of the pointing throughout the measurement period.

The results of the drone pointing verification are provided in Tables 7 and 8. To put these results into context, the elevation angle θ difference found using the drone method ranges between $-0.2°$ and $0.15°$, which corresponds to a height error in the lidar's beam position of between -3.9 and 3.0 m at intersection point C depicted in Figure 1. This range of errors is negligible considering the vertical scales of interest in this study.

2.3.3 Sea surface levelling verification

A further method to independently verify the correct levelling and range reference of the lidars is by scanning the sea-surface (either using PPI or RHI scans). Due to the narrow visibility of the water surface from the lidar positions, we used the RHI scans to determine the distance to the water, r_{ss} as a function of elevation angle, θ_{ss}, in this campaign. The method for finding the distance to the sea surface at each elevation angle, described in (Gramitzky et al., 2024), uses an inverse sigmoid function combined with a slope to fit to the CNR data at each elevation angle. A vertical cross section of the land, sea, and sky was scanned by each lidar. The curve of signal reflectivity (CNR) across distance inflects at the elevation position corresponding

https://doi.org/10.5194/wes-2026-39
Preprint. Discussion started: 23 February 2026

eawe european academy of wind energy
Open Access WIND ENERGY SCIENCE DISCUSSIONS

Table 7. Table of results from drone pointing verification at the start of the measurement campaign (February 8, 2024).

Scanner Name	ϕ global	ϕ found	ϕ difference	ϕ precision	θ global	θ found	θ difference	θ precision
				all variables in °				
Sterenn	314.24	314.63	0.39	0.3	5.75	5.64	-0.11	0.2
Zonda	304.79	304.88	0.09	0.2	6.57	6.37	-0.2	0.13
Chinook	311.92	311.77	-0.15	0.2	5.98	5.97	-0.01	0.08
Brise	221.92	221.88	-0.04	0.09	5.18	5.04	-0.14	0.04
Storm	226.65	226.75	0.10	0.14	5.66	5.81	0.15	0.05

Table 8. Table of results from drone pointing verification at the end of the measurement campaign (June 25, 2024).

Scanner Name	ϕ set	ϕ found	ϕ difference	ϕ precision	θ set	θ found	θ difference	θ precision
				all variables in °				
Sterenn	314.22	314.34	0.12	0.12	10.30	10.25	-0.05	0.03
Zonda	304.86	304.89	0.03	0.11	11.83	11.91	0.08	0.03
Chinook	311.92	311.81	-0.11	0.11	10.72	10.67	-0.05	0.01
Brise	221.92	221.88	-0.04	0.10	9.94	10.01	0.07	0.02
Storm	226.59	226.87	0.28	0.10	10.78	10.90	0.12	0.03

to the water surface, as depicted in Figure 8 which shows a single example from Chinook where the water surface was found at 1000 m for the corresponding elevation angle. Using this principle with multiple RHI scans repeated at the same azimuth angle provides a linear fit result such as the one shown in Figure 9 for Zonda. Here, the vertical and horizontal distances, from the scanner head to the sea surface, D_v and D_h, are calculated as

$$D_v = r_{ss} \sin\theta_{ss} \tag{2}$$

$$D_h = r_{ss} \cos\theta_{ss} \tag{3}$$

For the longer ranges used here, it is also necessary to correct for the effect of the curvature of the Earth. Here the vertical distance is corrected by Δh, which for horizontal distances much smaller than the radius of the earth, r_{earth}, is written as:

$$\Delta h = r_{\text{earth}} \left(1 - \cos\left(\frac{D_h}{r_{\text{earth}}}\right)\right) \tag{4}$$

The elevation error of the scanner in radians is given as the slope of the linear fit shown in Figure 9. It is possible to further extend this method across multiple azimuth positions to obtain tilt, roll, and range offset results for each lidar, however it was not necessary to do so in this campaign due to the configuration of the lidars being used to stare at a single position. The sea

https://doi.org/10.5194/wes-2026-39
Preprint. Discussion started: 23 February 2026

eawe european academy of wind energy
Open Access WIND ENERGY SCIENCE DISCUSSIONS

Table 9. Results from the sea surface RHI scans.

	Elevation error [°]	
Name	April 2024	June 2024
Zonda	−0.41	−0.30
Chinook	−0.12	−0.10
Sterenn	−0.12	No data
Storm	−0.02	−0.02
Brise	−0.18	−0.08

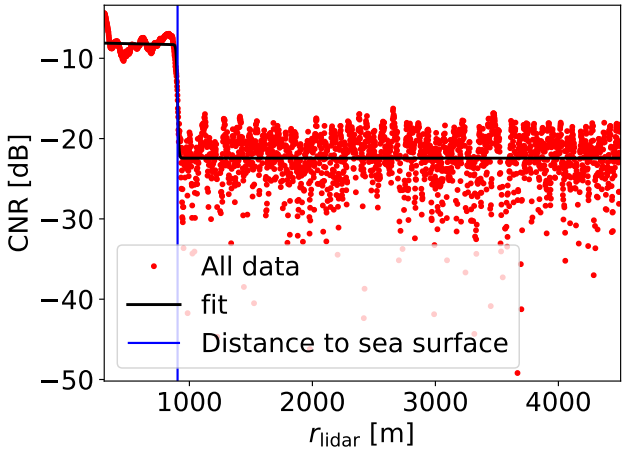

Figure 8. Single SSL measurement point from Chinook, showing the CNR value as a function of distance where the water surface is identified at 1000 m for the corresponding elevation angle.

surface levelling exercise was repeated twice during the campaign. The results from the two sea surface levelling exercises are shown in Table 9. In the results from April 2024, the elevation error found on Zonda was so large that it was decided to correct the elevation angle of the lidar in phase 2 of the experiment, using the results from April 2024 listed in Table 9.

2.3.4 Post-campaign LOS speed inter-comparison and offset verification

The final quality control effort took place at the end of the field campaign, which evaluated each lidar's line-of-sight speed offset, and the relative LOS speeds measured by lidars at the same deployment site. This test would either demonstrate that the systems were measuring the correct speeds consistent with the pre-campaign test results, or that an issue had occurred which would require a correction to the lidar data. This test was carried out in two phases.

https://doi.org/10.5194/wes-2026-39
Preprint. Discussion started: 23 February 2026

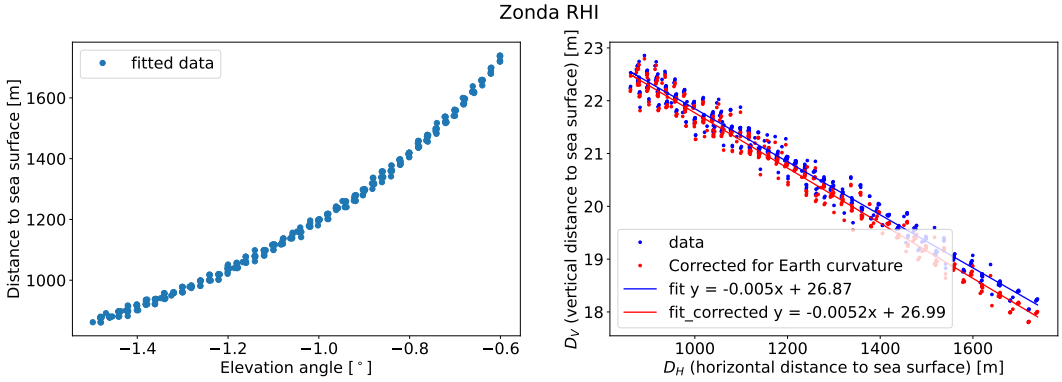

Figure 9. Results from repeated SSL RHI scans from Zonda at a single azimuth position. The distance to the sea surface was found using the method shown in Figure 8.

Table 10. Results from the post-campaign line-of-sight speed comparison between lidars at each site.

Scanner	LOS speed offset [m/s]
Chinook - Sterenn	−0.66
Chinook - Zonda	−0.11
Zonda - Sterenn	−0.57
Storm - Brise	−0.38

Phase 1 involved pointing each lidar beam at a fixed hard target (the church and lighthouse buildings were used via hard-target mapping) where the velocity of the buildings is known to be zero. The measured LOS speeds of each lidar were then evaluated to determine if there was a non-zero offset present. For the StreamLine systems this was not possible, due to saturation of the receiving sensor. For the Windscanner systems the results did not indicate a disagreement from the results obtained in the pre-campaign testing.

Phase 2 involved grouping the systems by deployment location (i.e. church vs. lighthouse), and performing an inter-comparison of measured LOS speeds between lidar pairs at the same site. This was done by placing the beams of all lidars at each site in parallel, and evaluating the independent observations of LOS speeds between all possible pairs of lidars at each location. Since the lidars were deployed next to each other and had their beams aligned in parallel, the measured values should be nearly identical. An important limitation of this approach is that since the two lidar groups are separated, it is not possible to make a meaningful comparison between lidars across the two sites. Applying a linear regression between observations of the lidar pairs provides a coefficient, offset and fit indicator of the agreement between the lidars. Figure 10 shows the LOS speed comparison between Brise and Storm for a single range, which is then extended across all ranges in Figure 11.

From the linear regression the offsets are averaged over all distances and shown in Table 10. The comparison involving Brise and Sterenn shows a significant offset compared to the comparison between Chinook and Zonda. The StreamLine scanners were sent to the factory for repair prior to the campaign, where they were tested against a reference lidar. These tests showed that the

https://doi.org/10.5194/wes-2026-39
Preprint. Discussion started: 23 February 2026

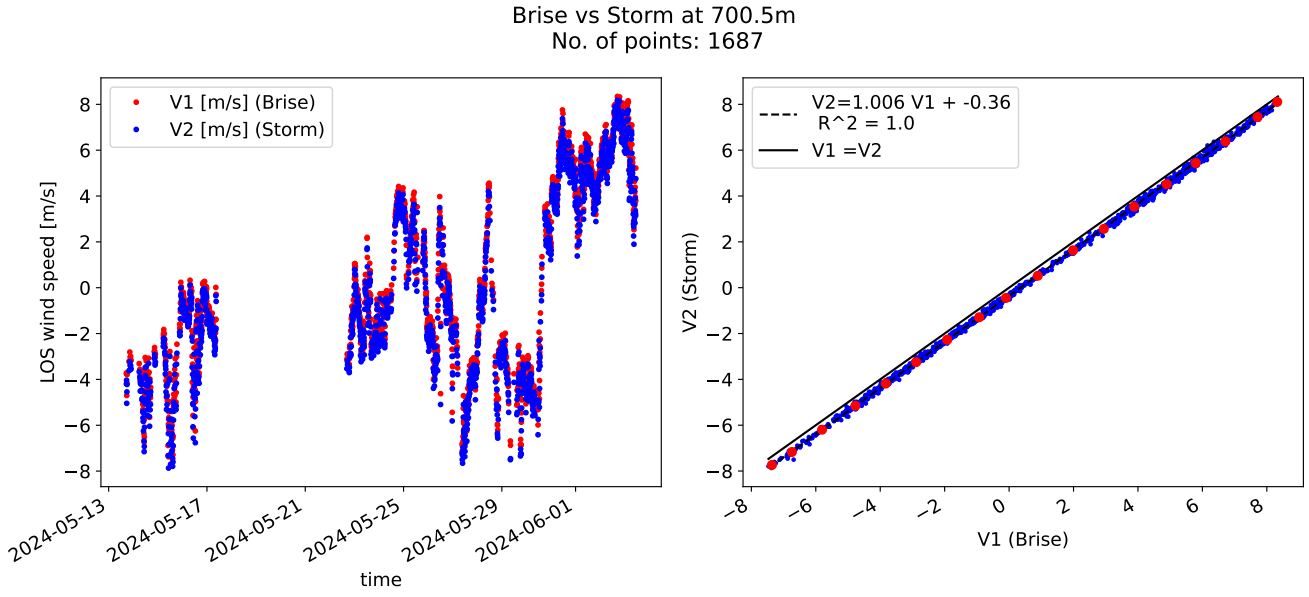

Figure 10. Post-campaign LOS speed inter-comparison between Brise and Storm at 700.5 m range. Time series (left) and binned linear regression (right, units on the axes are in m/s) with fit parameters.

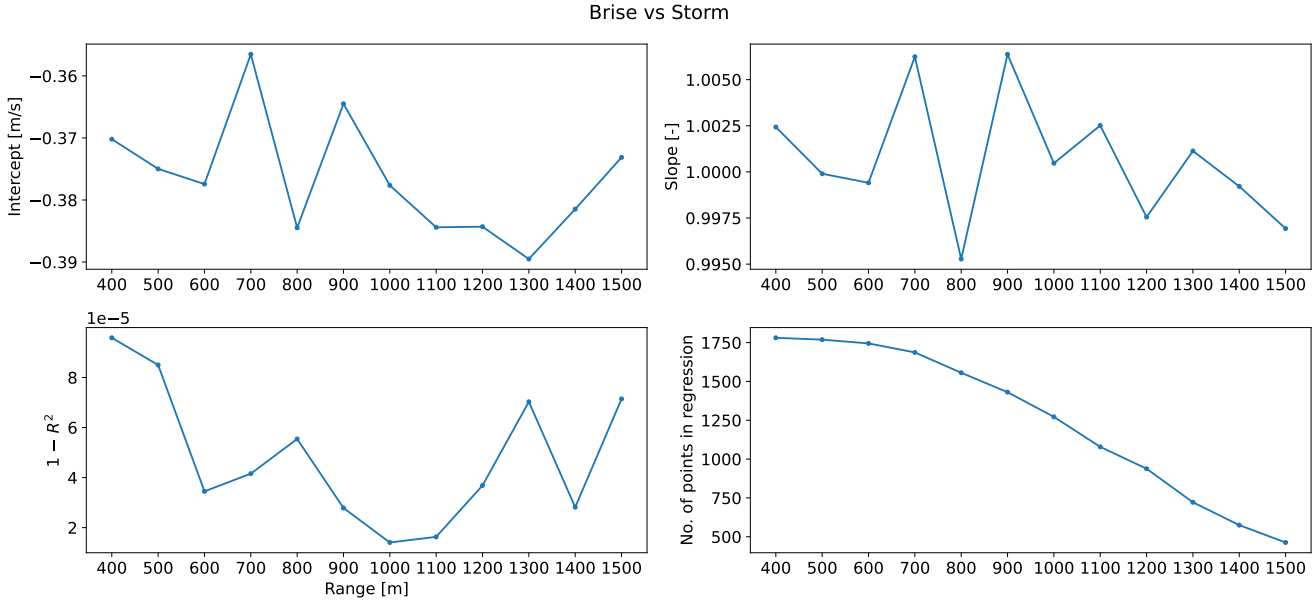

Figure 11. Linear fit parameters of post-campaign LOS speed inter-comparison between Brise and Storm across all ranges indicating good agreement between the two systems.

https://doi.org/10.5194/wes-2026-39
Preprint. Discussion started: 23 February 2026

eawe european academy of wind energy
Open Access WIND ENERGY SCIENCE DISCUSSIONS

Table 11. Final, recommended velocities to be added to the line-of-sight velocities for each lidar.

Scanner	LOS speed offset [m/s]
Sterenn	-0.7 m/s
Zonda	0 m/s
Chinook	0 m/s
Brise	-0.4 m/s
Storm	0 m/s

StreamLine units (Chinook and Storm) did not exhibit any significant LOS speed offsets. Considering this, the offsets identified in the post-campaign LOS speed calibration are primarily attributed to Brise and Sterenn, with magnitudes of approximately -0.4 m/s for Brise and -0.7 m/s for Sterenn. When compared with the pre-campaign test results, the findings are consistent in the sense that Sterenn shows a larger offset than Brise. Both offsets are substantial and should be corrected for during data analysis. A smaller offset of about 0.1 m/s is observed between Zonda and Chinook, but because the data will be used for turbulence analysis, this discrepancy is less critical. The final, recommended offsets are shown in Table

3 Data description

This section describes what is contained in the publicly available data repository (Patel et al., 2025). The following variables are present in the dataset:

1. Radial velocity: the measured wind speed along the lidar beam in m s^{-1}. It is measured at a frequency of 2 Hz (except for Zonda which measured at 1 Hz). Moreover, the radial velocity measurements are taken at multiple points along the lidar beam. These points are commonly referred to as range gates. Table 3 provides information on the range gates of each lidar.

2. Quantification of noise: The definition of noise in the radial velocity measurement differs for the five lidars. In the case of Zonda, Sterenn and Brise, it is quantified using the signal to noise ratio (SNR) expressed in decibels. On the other hand, the noise in Chinook and Storm is quantified using Streamline intensity (s), which can be related to the SNR as follows:

$$SNR = 10\log_{10}(s-1)\mathrm{dB}. \tag{5}$$

   Note that both SNR and s are measured at all range gates and at the same frequency as the radial velocity measurements.

3. Ceilometer data: The ceilometer data contain the aerosol backscatter signal sampled every 16 s and at a vertical resolution of 10 m. We refer the reader to Vaisala's technical documentation of the CL31 ceilometer for a more in depth description of the other data available from this device (CL3).

https://doi.org/10.5194/wes-2026-39
Preprint. Discussion started: 23 February 2026

eawe european academy of wind energy
Open Access WIND ENERGY SCIENCE DISCUSSIONS

Note that the dataset covers the entire period of the campaign from February 2024 to June 2024 while the periods corresponding to intra-campaign calibration (cf. Table 1) are not included. Thus, the data can be read by selecting the required time period and the range gate. We recommend using the scripts provided here. Moreover, offsets of -0.66 m/s and -0.38 m/s must be added to the data from Sterenn and Brise respectively.

4 Quality control of the campaign dataset

This section presents the post-processing of the raw lidar data in order to describe its quality. Note that the offsets shown in Table 11 were added to the data after reading from the raw dataset. We first define a filtering criterion to separate good and bad data. The latter is a result of many spikes being present in the time series due to low concentration of aerosols in the atmosphere, dirt on the lens, presence of obstacles in the lidar beam, etc (Vasiljević et al., 2016). The complete removal of noisy data, that is, the full 10-minute period, is necessary when analysing turbulence spectra or coherence because noise removal algorithms might introduce too many gaps (Beck and Kühn, 2017). In the literature, noise is often characterized by the carrier-to-noise ratio (CNR) and a flat threshold is applied on it to differentiate between reliable and unreliable data. But the so-called CNR filter suffers from many drawbacks, the most important one being the dependence of the optimal CNR threshold on the site conditions, instrument manufacturer, and experimental setup (Gryning et al., 2016). Indeed, we observed that the CNR threshold varied significantly with the atmospheric conditions. Thus, we choose to characterize the noise by another metric, the standard deviation of the radial velocities calculated over 10 minutes: σ_{v_r}. We found that it is easier to establish the optimal threshold for σ_{v_r} as it is mostly independent of the aforementioned factors.

After careful analysis of the data, we concluded that when σ_{v_r} is greater than 4 m s^{-1}, the 10 min period contains too many spikes. This threshold was determined by analysing many 10 min time series from the five lidars. Consequently, the corresponding 10 min periods were rejected. On the other hand, when σ_{v_r} is less than 1.2 - 1.5 m s^{-1}, depending on the lidar model, the 10 min period is free from spikes. And for those 10 min periods where σ_{v_r} is between 1.5 and 4 m s^{-1}, it is possible to remove spikes using a de-spiking algorithm such as the one described by Beck and Kühn (2017) without introducing too many gaps. As an example, we show time series from all five lidars in Fig. 12. The data on the right-hand side have many spikes with σ_{v_r} being greater than 4 m s^{-1}. While the data on the left-hand side is relatively free from noise and σ_{v_r} is lower than 1.2 m s^{-1}. The de-spiking algorithm developed by Beck and Kühn (2017) uses two-dimensional kernel density estimation (KDE) to find “data-dense" regions which are assumed to be free from noise. We used a modified version of the KDE filter to estimate the distribution of Δv_r instead of v_r, where:

$$\Delta v_r^t = v_r^t - v_r^{t-1} \tag{6}$$

and t represents the indexing of different samples in time.

https://doi.org/10.5194/wes-2026-39
Preprint. Discussion started: 23 February 2026

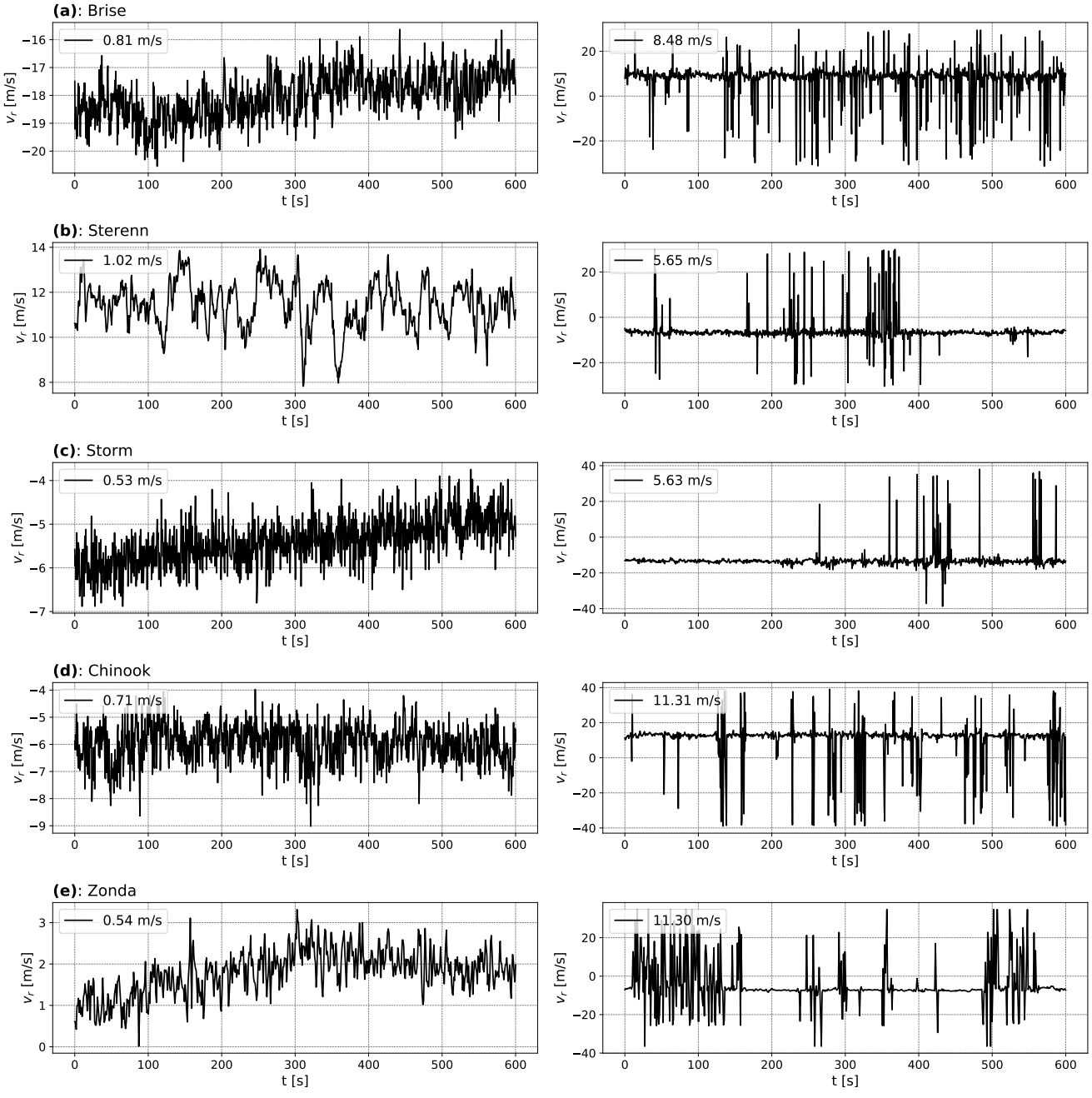

Figure 12. Some 10 min time series from all five lidars showing periods with good data (left) and bad data (right) characterized by σ_{v_r}.

https://doi.org/10.5194/wes-2026-39
Preprint. Discussion started: 23 February 2026

eawe european academy of wind energy
Open Access WIND ENERGY SCIENCE DISCUSSIONS

Next, we reconstructed the east-west (v_{EW}) and north-south (v_{NS}) wind components at the six crossing points using the following relations (Peña and Mann, 2019):

$$\underbrace{\begin{bmatrix} v_{r_1} \\ v_{r_2} \end{bmatrix}}_{\mathbf{v_r}} = \underbrace{\begin{bmatrix} \cos\phi_1 \cos\psi_1 & \sin\phi_1 \cos\psi_1 \\ \cos\phi_2 \cos\psi_2 & \sin\phi_2 \cos\psi_2 \end{bmatrix}}_{\mathbf{M}} \underbrace{\begin{bmatrix} v_{EW} \\ v_{NS} \end{bmatrix}}_{\mathbf{v}}, \tag{7}$$

and,

$$\mathbf{v} = \mathbf{M}^{-1}\mathbf{v_r}. \tag{8}$$

The subscripts 1 and 2 refer to the lidars close to the church and lighthouse, respectively, whereas ϕ is the azimuthal orientation of the beam and ψ is its elevation. Equation (7) relies on the assumption that the projection of the vertical wind component along the lidar beam is negligible. Given the small elevation angles of the beams, this assumption is justified. Since the beams of the church and lighthouse lidars are approximately 90° apart, when using Eq. (7) and Eq. (8), the uncertainty becomes almost independent of the wind direction (Peña and Mann, 2019). However, Eq. (7) implicitly introduces another filter criterion: data from two lidars must be available simultaneously. Data availability after applying the σ_{v_r} and modified KDE filters is not uniform across the five lidars. Some lidars provided noisier data than the rest, probably because they were older models (Sterenn) or had accumulated more dirt on the lens (Chinook). This can be seen in Fig. 13 where Storm, Zonda, and Brise have a lot more 10 min periods with σ_{v_r} between 0 to 2 m s^{-1}. Thus, the data availability is lowered when reconstructing the true wind vector, especially at crossing points with Sterenn and Chinook. This lidar pair has a joint availability of 17% while Zonda and Storm has the highest joint availability of 50%.

Subsequently, we computed the horizontal wind speed, u_{hor}:

$$u_{hor} = \sqrt{v_{EW}^2 + v_{NS}^2}, \tag{9}$$

and the wind direction, θ:

$$\theta = \arctan\left(-v_{EW}, -v_{NS}\right). \tag{10}$$

Note that this wind direction is expressed in the meteorological convention, where 0° is aligned with true North and increases in the clockwise sense, and that the first argument in the $\arctan$ function is "y" ("opposite"). The histograms of the 10 min mean horizontal wind speed (U_{hor}) and wind direction (Θ) are shown in Fig. 14 and Fig. 15, respectively. The modal 10 min wind speed is between 11 and 12 m s^{-1} and the maximum observed value of U_{hor} was 26.2 m s^{-1}. The modal wind direction was between 210° to 220° from the start of the campaign to the end of April 2024, while from May 2024 to the end of the campaign, it was between 290° and 300°. This corresponds to westerly circulation over the northern mid-latitudes due to the Ferrel cell. Easterly winds are also frequently observed, but the data areaffected by the terrain.

We also reconstructed the mean vertical profiles of the wind speed using data from many range gates and assuming horizontal homogeneity. This assumption is valid for westerly winds averaged over a large period of time. The profiles from four different

https://doi.org/10.5194/wes-2026-39
Preprint. Discussion started: 23 February 2026

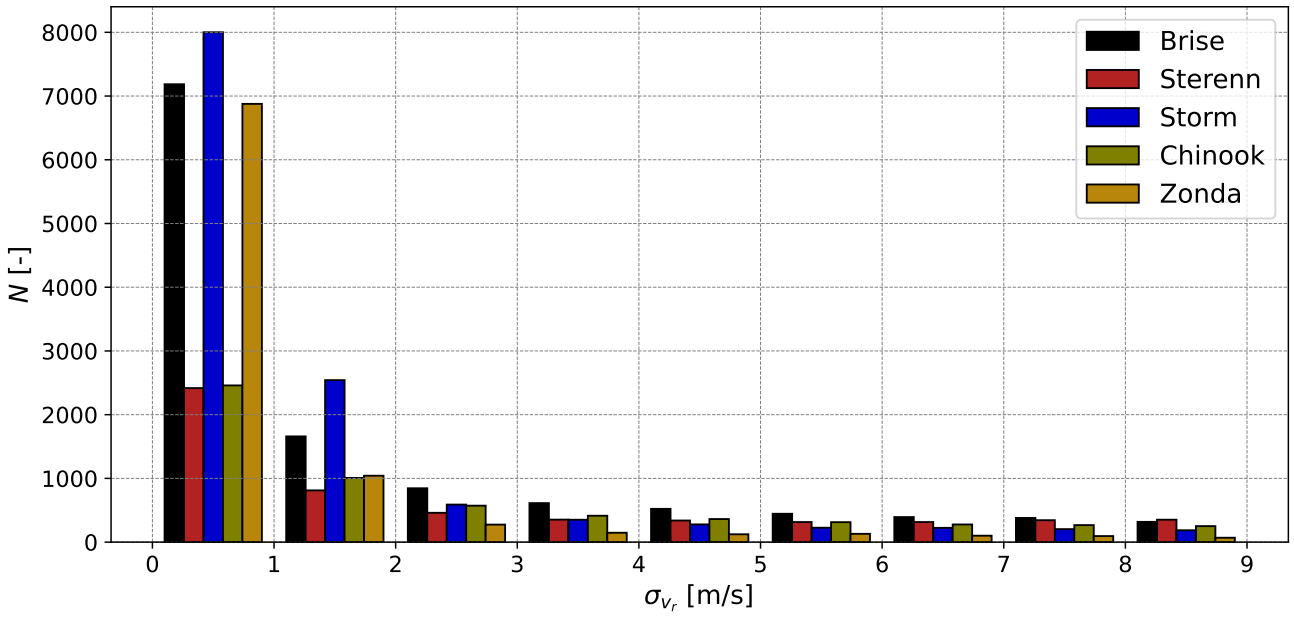

Figure 13. Histogram of σ_{v_r} for the five lidars using data from one of the range gates present at the intersection points.

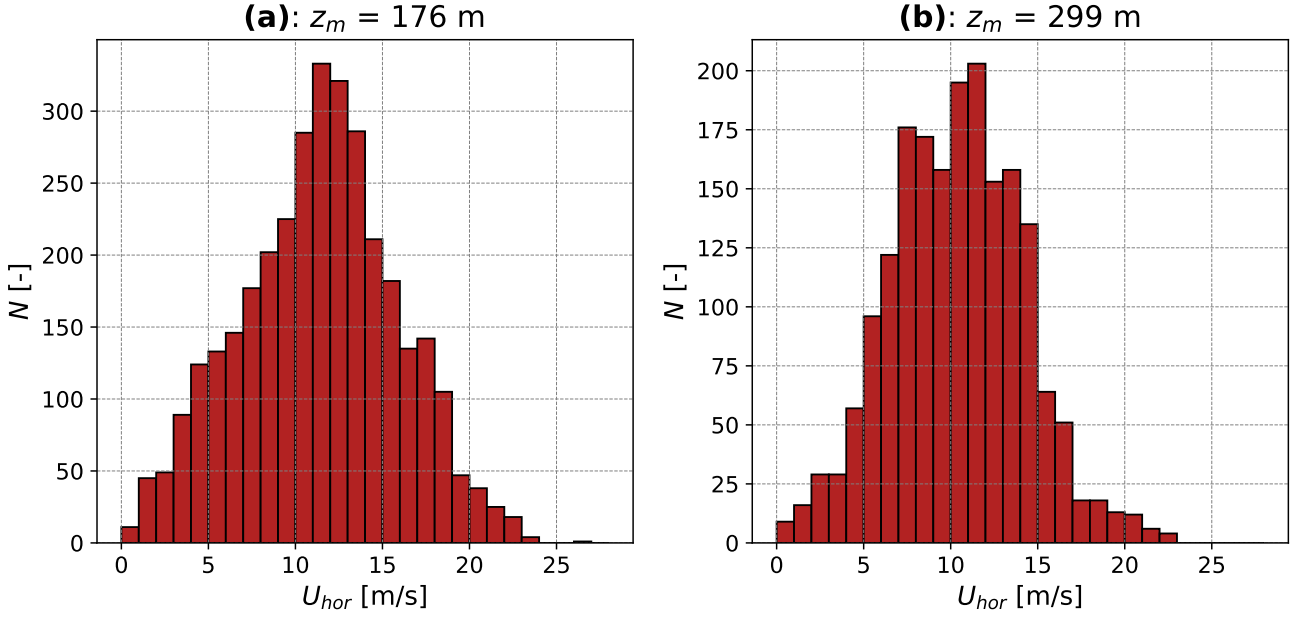

Figure 14. Histogram of the 10 min mean wind speed at point 2 in beam direction 1 (a) and 2 (b).

https://doi.org/10.5194/wes-2026-39
Preprint. Discussion started: 23 February 2026

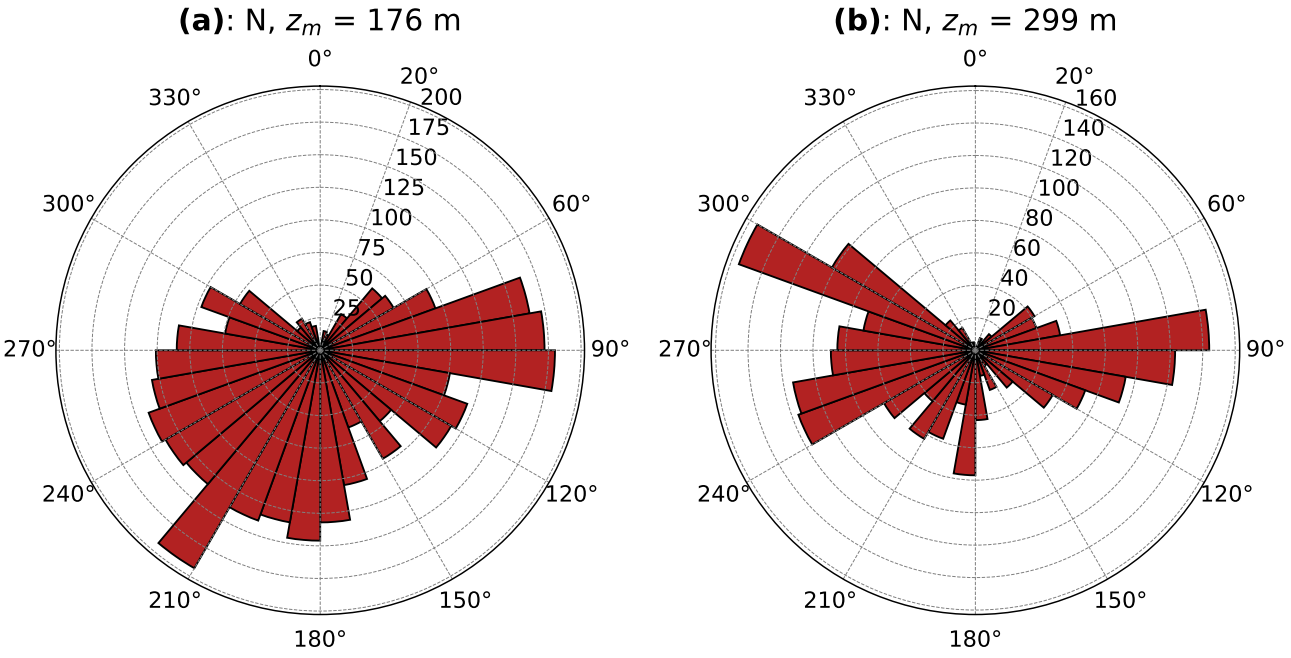

Figure 15. Histogram of the 10 min mean wind direction in polar coordinates at point 2 in beam direction 1 (a) and 2 (b).

Table 12. Time periods over which the wind speed profiles were averaged in figure 16

Sub-figure	Time period
(a)	16 March 2024 04:00 UTC to 07:30 UTC
(b)	15 March 2024 02:30 UTC to 08:40 UTC
(c)	16 February 2024 21:50 UTC to 23:20 UTC
(d)	21 March 2024 04:30 UTC to 07:00 UTC

periods, as described in Table 12, are shown in Fig. 16. As a sanity check, we also compare the measured profiles to those obtained from Weather Research and Forecast (WRF) simulations (Wang et al., 2010) carried out by Olsen et al. (2024). We used the data from the simulations with the 3DTKE PBL scheme and extracted a column of wind speeds from the grid point closest to the intersection plane of the lidars. This configuration was used as Olsen et al. (2024) found that it performed best at capturing the wind profile.

Figure 16 shows good agreement between the wind speed profiles from WRF and the measurements, although with an offset of approximately 1 m s^{-1}. Similar results have been obtained when comparing wind profiles from WRF with either met mast or lidar measurements (Floors et al., 2013; Svensson et al., 2019). We observed a better agreement in periods with neutral stratification ((a) and (c)) in contrast to stable (b) and unstable (d) stratifications.

https://doi.org/10.5194/wes-2026-39
Preprint. Discussion started: 23 February 2026

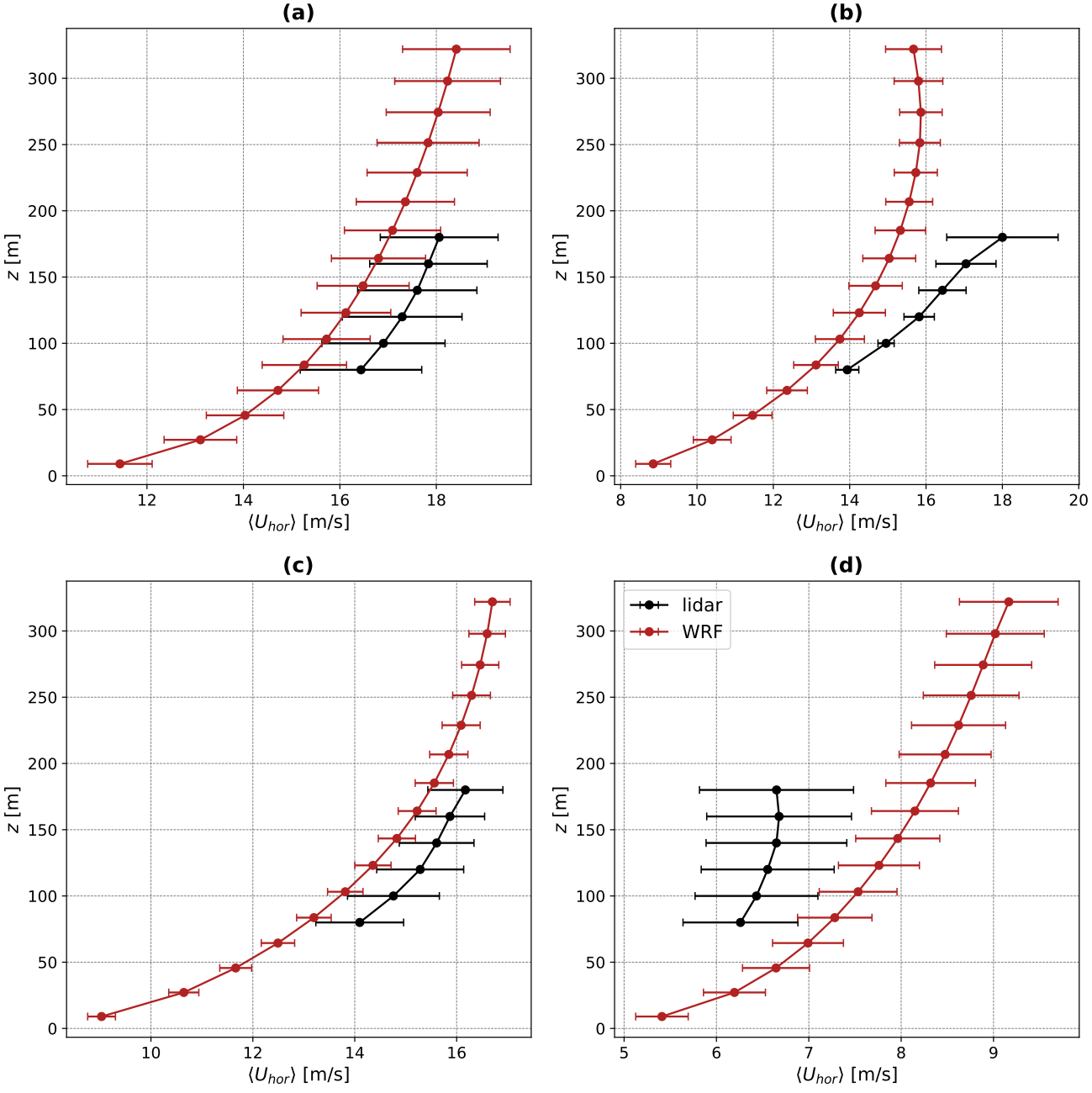

Figure 16. Profiles of the horizontal wind speed averaged over four different periods (shown in table 12) from the lidar measurements and WRF simulation. The error bars indicate the standard deviation of the wind speed.

https://doi.org/10.5194/wes-2026-39
Preprint. Discussion started: 23 February 2026

eawe european academy of wind energy
Open Access WIND ENERGY SCIENCE DISCUSSIONS

The analysis presented above shows that the campaign data is of good quality and can be used for the statistical analysis of turbulence in the marine boundary layer.

5 Conclusions

A measurement campaign that recorded the horizontal wind components at 150 m to 250 m above the sea was presented. The experiment used five lidars placed along the west coast of Denmark, with their beams intersecting in a close-to-horizontal plane. This allowed the wind data to be measured concurrently at six different points from which the lateral coherence could be computed. The lidars were calibrated before, during, and after the experiment via a few different methods which included the usage of drones, sea-surface levelling and hard target mapping. We also described the storage format of the data and how it can be retrieved for further analysis. Quality checks on the lidar data showed that two instruments suffered from poor signal quality, which lowered the data availability at the respective intersection points. The 10 min statistics of the wind speed and direction followed the trends expected at the geographic location of the site. The wind profiles reconstructed from the lidar data showed good agreement with WRF simulations. Thus, the measurements can be used to analyse auto-spectra and lateral coherence at heights relevant for offshore wind turbines and validate newer turbulence models, as shown in Patel et al. (2026). The dataset could also be used to study wind profiles and gusts in the MBL.

Code availability. The code used to read the raw lidar data can be found here: https://data.dtu.dk/articles/dataset/Trans_experiment_data_paper_script/29224631.

Data availability. The raw lidar data is available from the following reference: Patel et al. (2025). Please cite the dataset using: Patel, Ansh; Simon, Elliot; Mann, Jakob; Sjöholm, Mikael; Rolighed Thorsen, Gunhild; Hung, Lin-ya; et al. (2025). Trans experiment (FLOW) - raw lidar data. Technical University of Denmark. Dataset. https://doi.org/10.11583/DTU.28749252.v2

Author contributions. The manuscript was prepared with contributions from all authors, with AP having the main responsibility. The experiment was designed by JM with inputs from MS and JG. GRT, ES, and LH were responsible for the installation, calibration, monitoring, and decommissioning of the instrumentation, as well as the data storage. AP carried out the quality checks on the data.

Competing interests. Two of the authors are chief editors of the Wind Energy Science journal, but were not involved in the editorial handling of this manuscript.

https://doi.org/10.5194/wes-2026-39
Preprint. Discussion started: 23 February 2026

Acknowledgements. We appreciate the support of the community at Trans Church. We further wish to express our gratitude to Dr. Michael Courtney from DTU for making this experiment possible. We would also like to acknowledge the technical staff at DTU including Anders Ramsing Vestergaard, Noah Nørgaard Soelberg, Allan Djernes Blaabjerg, Lars Christensen, Michael Sejer Rasmussen, and Per Hansen for their contributions and assistance in installing and supporting the experiment, and to Mathieu Pellé for his technical assistance in processing the drone data. This project is funded through the European Union Horizon Europe Framework programme HORIZON-CL5-2021-D3-03-04 under grant agreement no. 101084205 (FLOW) and HORIZON-MSCA-2022-DN-01 under grant agreement no. 101119550 (AptWind).

https://doi.org/10.5194/wes-2026-39
Preprint. Discussion started: 23 February 2026

References

CL31 User guide Reader Product documentation portal, https://docs.vaisala.com/r/M210482EN-L/en-US.

Danmarks Højdemodel - Højdekurver, https://dataforsyningen.dk/data/926.

Angelou, N., Mann, J., and Dubreuil-Boisclair, C.: Revealing inflow and wake conditions of a 6 MW floating turbine, Wind Energy Science, 8, 1511–1531, https://doi.org/10.5194/WES-8-1511-2023, 2023.

Beck, H. and Kühn, M.: Dynamic Data Filtering of Long-Range Doppler LiDAR Wind Speed Measurements, Remote Sensing 2017, Vol. 9, Page 561, 9, 561, https://doi.org/10.3390/RS9060561, 2017.

Cheynet, E., Jakobsen, J. B., Snæbjörnsson, J., Mikkelsen, T., Sjöholm, M., Mann, J., Hansen, P., Angelou, N., and Svardal, B.: Application of short-range dual-Doppler lidars to evaluate the coherence of turbulence, Experiments in Fluids, 57, 1–17, https://doi.org/10.1007/S00348-016-2275-9/FIGURES/15, 2016.

Cheynet, E., Jakobsen, J. B., and Obhrai, C.: Spectral characteristics of surface-layer turbulence in the North Sea, Energy Procedia, 137, 414–427, https://doi.org/10.1016/J.EGYPRO.2017.10.366, 2017.

Cheynet, E., Jakobsen, J. B., and Reuder, J.: Velocity Spectra and Coherence Estimates in the Marine Atmospheric Boundary Layer, Boundary-Layer Meteorology, 169, 429–460, https://doi.org/10.1007/S10546-018-0382-2/TABLES/3, 2018.

Cheynet, E., Flügge, M., Reuder, J., Jakobsen, J. B., Heggelund, Y., Svardal, B., Garfias, P. S., Obhrai, C., Daniotti, N., Berge, J., Duscha, C., Wildmann, N., Onarheim, I. H., and Godvik, M.: The COTUR project: Remote sensing of offshore turbulence for wind energy application, Atmospheric Measurement Techniques, 14, 6137–6157, https://doi.org/10.5194/AMT-14-6137-2021, 2021.

Chougule, A., Mann, J., Kelly, M., and Larsen, G. C.: Modeling atmospheric turbulence via rapid distortion theory: spectral tensor of velocity and buoyancy, Journal of the Atmospheric Sciences, 74, 949–974, 2017.

Davenport, A. G.: The spectrum of horizontal gustiness near the ground in high winds, Quarterly Journal of the Royal Meteorological Society, 87, 194–211, https://doi.org/10.1002/qj.49708737208, 1961.

Floors, R., Vincent, C. L., Gryning, S., Peña, A., and Batchvarova, E.: The Wind Profile in the Coastal Boundary Layer: Wind Lidar Measurements and Numerical Modelling, Boundary-Layer Meteorology, 147, 469–491, https://doi.org/10.1007/S10546-012-9791-9/FIGURES/10, 2013.

Floors, R., Peña, A., Lea, G., Vasiljević, N., Simon, E., and Courtney, M.: The RUNE experiment—A database of remote-sensing observations of near-shore winds, Remote Sensing, 8, 884, 2016.

Gramitzky, K., Jäger, F., Hildebrand, T., Gloria, N., Riechert, J., Steger, M., and Pauscher, L.: Alignment calibration and correction for offshore wind measurements using scanning lidars, Journal of Physics: Conference Series, 2767, 042 014, https://doi.org/10.1088/1742-6596/2767/4/042014, 2024.

Gryning, S. E., Floors, R., Peña, A., Batchvarova, E., and Brümmer, B.: Weibull Wind-Speed Distribution Parameters Derived from a Combination of Wind-Lidar and Tall-Mast Measurements Over Land, Coastal and Marine Sites, Boundary-Layer Meteorology, 159, 329–348, https://doi.org/10.1007/S10546-015-0113-X/FIGURES/11, 2016.

International Electrotechnical Commission: IEC 61400-50-3:2022 Wind energy generation systems: Part 50-3: Use of nacelle-mounted lidars for wind measurements, 2022.

Kaimal, J. C., Wyngaard, J. C., Izumi, Y., and Coté, O. R.: Spectral characteristics of surface-layer turbulence, Quarterly Journal of the Royal Meteorological Society, 98, 563–589, https://doi.org/10.1002/QJ.49709841707, 1972.

https://doi.org/10.5194/wes-2026-39
Preprint. Discussion started: 23 February 2026

Kuik, G. A. V., Peinke, J., Nijssen, R., Lekou, D., Mann, J., Sørensen, J. N., Ferreira, C., Wingerden, J. W. V., Schlipf, D., Gebraad, P., Polinder, H., Abrahamsen, A., Bussel, G. J. V., Sørensen, J. D., Tavner, P., Bottasso, C. L., Muskulus, M., Matha, D., Lindeboom, H. J., Degraer, S., Kramer, O., Lehnhoff, S., Sonnenschein, M., Sørensen, P. E., Künneke, R. W., Morthorst, P. E., and Skytte, K.: Long-term research challenges in wind energy – a research agenda by the European Academy of Wind Energy, Wind Energy Science, 1, 1–39, https://doi.org/10.5194/WES-1-1-2016, 2016.

Lampert, A., Bärfuss, K., Platis, A., Siedersleben, S., Djath, B., Cañadillas, B., Hunger, R., Hankers, R., Bitter, M., Feuerle, T., et al.: In situ airborne measurements of atmospheric and sea surface parameters related to offshore wind parks in the German Bight, Earth System Science Data, 12, 935–946, 2020.

Larsén, X. G., Vincent, C., and Larsen, S.: Spectral structure of mesoscale winds over the water, Quarterly Journal of the Royal Meteorological Society, 139, 685–700, https://doi.org/10.1002/QJ.2003, 2013.

Lenschow, D. H. and Agee, E.: Preliminary results from the air mass transformation experiment (AMTEX), Bulletin of the American Meteorological Society, 57, 1346–1355, 1976.

Lenschow, D. H. and Stankov, B. B.: Length scales in the convective boundary layer, Journal of Atmospheric Sciences, 43, 1198–1209, 1986.

Lindborg, E.: Can the atmospheric kinetic energy spectrum be explained by two-dimensional turbulence?, Journal of Fluid Mechanics, 388, 259–288, https://doi.org/10.1017/S0022112099004851, 1999.

Mann, J.: The spatial structure of neutral atmospheric surface-layer turbulence, Journal of Fluid Mechanics, 273, 141–168, https://doi.org/10.1017/S0022112094001886, 1994.

Mann, J., Kristensen, L., and Courtney, M.: The Great Belt coherence experiment. A study of atmospheric turbulence over water, no. 596(EN) in Denmark. Forskningscenter Risoe. Risoe-R, ISBN 87-550-1747-9, 1991.

Nafisifard, M., Jakobsen, J. B., Snæbjörnsson, J. T., Sjöholm, M., and Mann, J.: Triple-lidar measurements of wind across a virtual rotor plane over a sea surface, Journal of Physics: Conference Series, 2626, 012 022, https://doi.org/10.1088/1742-6596/2626/1/012022, 2023.

Nastrom, G., Gage, K., and Jasperson, W.: Kinetic energy spectrum of large-and mesoscale atmospheric processes, Nature, 310, 36–38, 1984.

Olsen, B. T. E., Hahmann, A. N., Alonso-de Linaje, N. G., Žagar, M., and Dörenkämper, M.: Low-level jets in the North and Baltic Seas: Mesoscale Model Sensitivity and Climatology, EGUsphere, 2024, 1–49, https://doi.org/10.5194/egusphere-2024-3123, 2024.

Patel, A., Simon, E., Mann, J., Sjöholm, M., Rolighed Thorsen, G., Hung, L.-Y., and Gottschall, J.: Trans experiment (FLOW) - raw lidar data, https://doi.org/https://doi.org/10.11583/DTU.28749252.v2, 2025.

Patel, A., Mann, J., Sjöholm, M., Thorsen, G. R., Syed, A. H., Simon, E. I., Hung, L.-Y., and Gottschall, J.: Lidar observations of turbulence for tall offshore wind turbines, Journal of Fluid Mechanics, 1028, A9, https://doi.org/10.1017/jfm.2025.11103, 2026.

Peña, A., Floors, R., Sathe, A., Gryning, S.-E., Wagner, R., Courtney, M. S., Larsén, X. G., Hahmann, A. N., and Hasager, C. B.: Ten years of boundary-layer and wind-power meteorology at Høvsøre, Denmark, Boundary-Layer Meteorology, 158, 1–26, 2016.

Peña, A. and Mann, J.: Turbulence Measurements with Dual-Doppler Scanning Lidars, Remote Sensing 2019, Vol. 11, Page 2444, 11, 2444, https://doi.org/10.3390/RS11202444, 2019.

Putri, R. M., Cheynet, E., Obhrai, C., and Jakobsen, J. B.: Turbulence in a coastal environment: the case of Vindeby, Wind Energy Science, 7, 1693–1710, 2022.

Sathe, A. and Mann, J.: A review of turbulence measurements using ground-based wind lidars, Atmospheric Measurement Techniques, 6, 3147–3167, https://doi.org/10.5194/amt-6-3147-2013, 2013.

Segalini, A. and Arnqvist, J.: A spectral model for stably stratified turbulence, Journal of Fluid Mechanics, 781, 330–352, 2015.

https://doi.org/10.5194/wes-2026-39
Preprint. Discussion started: 23 February 2026

Simon, E., Courtney, M., Cassamo, N., Hrywniack, E., Delbos, F., Champneys, D., Lu, W., Sathiyanarayanan, D., Rodaway, C., and Adams, N.: OWA GloBE: The importance of pre- and post-campaign lidar calibrations, windEurope 2023 ; Conference date: 25-04-2023 Through 27-04-2023, 2023.

Sogachev, A. and Dellwik, E.: Flux footprints for a tall tower in a land–water mosaic area: A case study of the area around the Risø tower, Agricultural and Forest Meteorology, 237, 326–339, 2017.

Svensson, N., Arnqvist, J., Bergström, H., Rutgersson, A., and Sahlée, E.: Measurements and Modelling of Offshore Wind Profiles in a Semi-Enclosed Sea, Atmosphere 2019, Vol. 10, Page 194, 10, 194, https://doi.org/10.3390/ATMOS10040194, 2019.

Syed, A. H. and Mann, J.: A Model for Low-Frequency, Anisotropic Wind Fluctuations and Coherences in the Marine Atmosphere, Boundary-Layer Meteorology, 190, 1–37, https://doi.org/10.1007/S10546-023-00850-W/FIGURES/21, 2024.

Thorsen, G., Simon, E., and Clausen, E.: Drone-based scanning lidar pointing calibration (D4.4), DTU Wind and Energy Systems, 2023.

Vasiljević, N., Lea, G., Courtney, M., Cariou, J.-P., Mann, J., and Mikkelsen, T.: Long-Range WindScanner System, Remote Sensing, 8, https://doi.org/10.3390/rs8110896, 2016.

Veers, P., Bottasso, C. L., Manuel, L., Naughton, J., Pao, L., Paquette, J., Robertson, A., Robinson, M., Ananthan, S., Barlas, T., Bianchini, A., Bredmose, H., Horcas, S. G., Keller, J., Madsen, H. A., Manwell, J., Moriarty, P., Nolet, S., and Rinker, J.: Grand challenges in the design, manufacture, and operation of future wind turbine systems, Wind Energy Science, 8, 1071–1131, https://doi.org/10.5194/WES-8-1071-2023, 2023.

Vincent, C. L., Larsén, X. G., Larsen, S. E., and Sørensen, P.: Cross-Spectra Over the Sea from Observations and Mesoscale Modelling, Boundary-Layer Meteorology, 146, 297–318, https://doi.org/10.1007/S10546-012-9754-1/METRICS, 2013.

Wang, W., Bruyere, C., Duda, M., Dudhia, J., Gill, D., Lin, H.-C., Michalakes, J., Rizvi, S., Zhang, X., Beezley, J. D., et al.: ARW version 3 modeling system user's guide. Mesoscale & Miscroscale Meteorology Division, National Center for Atmospheric Research, 312, 2010.

Weiler, H. S. and Burling, R. W.: Direct Measurements of Stress and Spectra of Turbulence in the Boundary Layer Over the Sea, Journal of Atmospheric Sciences, 24, 653 – 664, https://doi.org/10.1175/1520-0469(1967)024<0653:DMOSAS>2.0.CO;2, 1967.

Wyngaard, J. C.: Atmospheric turbulence, Annu. Rev. Fluid Mech, 205, 33, 1992.